Title

Raytracing Monte Carlo Method for calculating Secondary Electron Emission and Sputtering Effects on Micro-Architected Structures

Author

Alvarado, Andrew

Publication Date

2019

Peer reviewed|Thesis/dissertation

UNIVERSITY OF CALIFORNIA
Los Angeles

Raytracing Monte Carlo Method for calculating Secondary Electron Emission and Sputtering Effects on Micro-Architected Structures

A thesis submitted in partial satisfaction
of the requirements for the degree
Master of Science in Material Science and Engineering

by

Andrew Michael Alvarado

2019

ABSTRACT OF THE THESIS

Raytracing Monte Carlo Method for calculating Secondary Electron Emission and Sputtering Effects on Micro-Architected Structures

by

Andrew Michael Alvarado
Master of Science in Material Science and Engineering
University of California, Los Angeles, 2019
Professor Jaime Marian, Chair

Secondary electron emission (SEE) from inner linings of plasma chambers in electric thrusters for space propulsion can have a disruptive effect on device performance and efficiency. SEE is typically calculated using elastic and inelastic electron scattering theory by way of Monte Carlo simulations of independent electron trajectories. However, in practice the method can only be applied for ideally smooth surfaces and thin films, not representative of real material surfaces. Recently, micro-architected surfaces with micron-sized features have been proposed to mitigate SEE and ion-induced erosion in plasma-exposed thruster linings. In this thesis, an approach is made for calculating secondary electron yields from surfaces with arbitrarily-complex geometries using an extension of the *ray tracing* Monte Carlo (RTMC) technique. Further, the model is extended to study the surface morphology evolution of micro-architectured foam samples due to plasma exposure. Microfoam structures are studied with varying porosities as representative micro-architected surfaces and use RTMC to generate primary electron or particle trajectories and track secondary electrons or particles until their escape from the outer surface. Actual surfaces are represented as a discrete finite element meshes obtained from X-ray tomography images of tungsten microfoams. At the local level, primary rays impinging into surface elements produce daughter rays of secondary electrons whose number, energies and angular characteristics are set by pre-calculated tables

of SEE yields and energies from ideally flat surfaces. Depending on porosity and primary electron energy, the micro-architected geometries can reduce SEE by up to 50% with respect to flat surfaces.

The thesis of Andrew Michael Alvarado is approved.

Nasr M. Ghoniem

Ya-Hong Xie

Jaime Marian, Committee Chair

University of California, Los Angeles

2019

To my parents . . .

who will always be my inspiration.

TABLE OF CONTENTS

LIST OF FIGURES

LIST OF TABLES

ACKNOWLEDGMENTS

I would like to express my deepest thanks to the opportunities and guidance given to me by my advisor and mentor Professor Jaime Marian. Additionally, I would like to thank the members of this thesis committee Professor Nasr Ghoniem and Professor Ya-Hong Xie for their time and guidance. Finally, I would like to acknowledge and thank Iris Chang and Warren Nadvornick for the many discussions and support related to this work, Iris for the physics behind the model and Warren for the geometry behind the model.

This work used computational and storage services associated with the Hoffman2 Shared Cluster provided by UCLA Institute for Digital Research and Educations Research Technology Group. The author acknowledges support from the Air Force Office of Scientific Research (AFOSR), through award number FA9550-11-1-0282 with UCLA.

VITA

2014 B.S. (Physics), University of Nevada, Las Vegas.

2016 M.S. (Physics), University of Nevada, Las Vegas.

PUBLICATIONS

Shanmin Wang, Jianzhong Zhang, Yi Zhang, Andrew Alvarado, Jeevake Attapattu, Duanwei He, Liping Wang, Changfeng Chen, Yusheng Zhao, "Phase-transition induced elastic softening and band gap transition in semiconducting PbS at hig pressure," Inorganic Chemistry 52, 8638 (2013).

Andrew Alvarado, Jeevake Attapattu, Yi Zhang, and Changfeng Chen, "Thermoelectric properties of rocksalt ZnO from first-principles calculations," Journal of Applied Physics 118, 1615101 (2015).

Alvarado, Andrew Michael, "High-Pressure Properties of Several Narrow Bandgap Semiconductors from First-Principles Calculations," UNLV Theses, Dissertations, Professional Papers, and Capstones, 2629 (2016).

Hsing-Yin Chang, Andrew Alvarado, and Jaime Marian, "Calculation of secondary electron emission yields from low-energy electron deposition in tungsten surfaces," Applied Surface Science 50, 190-199, (2018).

Andrew Alvarado, Hsing-Yin Chang, Warren Nadvornick, Nasr Ghoniem, and Jaime Marian, "Monte Carlo raytracing method for calculating secondary electron emission from micro-

architected surfaces," Applied Surface Science 478, 142-149 (2019).

Hsing-Yin Chang, Andrew Alvarado, Trey Weber, Jaime Marian, "Monte Carlo modeling of low-energy electron-induced secondary electron emission yields in micro-architected boron nitride surfaces," Nuclear Instruments and Methods in Physics Research Section B: Beam Interactions with Materials and Atoms 454, 14-22 (2019).

CHAPTER 1

Introduction

The release of electrons from a material surface exposed to a primary electron beam, known as secondary electron emission (SEE), is an important phenomenon with applications in a wide variety of physical processes, such as in electron multiplication devices [1, 2], electron microscopes [3, 4], and plasma devices [5, 6, 7, 8, 9, 10, 11, 12], among others. While SEE can be induced to amplify electron currents, such as during photoemission spectroscopy [13], it can also be detrimental for performance, such as in the case of the *multipactor* effect in radio frequency devices [14].

In the case of Hall thrusters for electric propulsion [8], an electrostatic sheath forms between the plasma and the inner lining of the plasma-facing surface material. This sheath potential acts as a thermal insulator and as a deterrent of current flow that protects the wall from particle discharges [15]. SEE weakens this sheath potential [15, 11, 12, 16], which has detrimental effects for the stability of the thruster, as is known to occur as well in magnetic fusion devices and radiofrequency plasma sources [9, 11]. Thus, as a crucial phenomenon affecting the efficiency of these devices, there is an increasing interest in mitigating –or at least controlling– secondary electron emission. A direct method to reduce the overall SEE yield is to engineer the structure of the material surface, leading to a class of surfaces known under the umbrella term of *microarchitected* surfaces.

Aside from early efforts in surface texture development to control SEE [17, 18], the use of advanced characterization and new processing techniques to develop microarchitected surfaces and experimentally determine the reduction in SEE yield is relatively recent [19, 20, 21]. There are now numerous examples of successful designs that are seen to lower

the secondary electron yield [22, 19, 23, 24]. These surfaces can be fabricated ex situ and deposited over existing chamber walls to achieve the desired level of functionalization.

The theory of secondary electron emission is generally well known and has been studied for decades [25, 26, 1]. However, studies of how the surface geometry and morphology affect the rate of electron emission are relatively limited. Modeling and simulation can play an important role in predicting the expected reduction rates of SEE before a costly effort of surface texture development, fabrication, and testing needs to be mounted. Simulations involving surfaces with grooves [27], 'velvet'-like fibers [20] and open-cell structures [21] have been recently carried out, showcasing the versatility of numerical simulation but also its relatively high computational cost. This thesis will present a two-pronged simulation approach in which SEE yields and energy spectra are precomputed for ideally flat surfaces, and are later used to describe the constitutive response at the local material point level of a discretized surface with arbitrary geometry. The connection between both descriptions is made via a ray-tracing Monte Carlo algorithm coupled to an intersection detection algorithm. The method simulates individual electron tracks, one at a time, and generates secondary tracks on the basis of incident energies and angles sampled from the precomputed physical relations. The number of tracks that escapes the surface is tallied and compared to the total number of simulated tracks to compute the effective secondary electron emission yield.

CHAPTER 2

Computational Model of Raytracing Monte Carlo

The raytracing monte carlo model is based on a raytracing method to track a ray trajectories from a random point above the surface as they are directed towards the material. This *primary* ray is defined by its energy E and angle of incidence with respect to a laboratory (global) frame of reference. Once this primary ray is generated, the next step is to determine whether its trajectory intersects the material surface, discretized into a finite element mesh, i.e. whether the ray crosses a surface element of the mesh. The algorithm used to detect such intersections is an extension of the Möller and Trumbore algorithm [28], which is briefly review in the following.

2.1 Intersection detection algorithm

Here a brief overview of the Möller-Trumbore (M-T) method [28] is explained. The procedure is described for triangular surface elements, although it can be extended to other geometric shapes in a straightforward manner. A ray defined by an origin $\boldsymbol{O}$ and a direction $\boldsymbol{D}$ is defined by the equation:

$$\boldsymbol{R}(t) = \boldsymbol{O} + t\boldsymbol{D} \tag{2.1}$$

where t is a scaling parameter that defines the length of the ray. If the vertices of the surface element triangle $\boldsymbol{V}_0, \boldsymbol{V}_1, \boldsymbol{V}_2$ are known, any point on the element can be defined by

$$\boldsymbol{T}(u, v) = (1 - u - v)\boldsymbol{V}_0 + u\boldsymbol{V}_1 + v\boldsymbol{V}_2. \tag{2.2}$$

Where u and v are barycentric coordinates that define the plane of a triangle, and satisfy $u \geq 0$, $v \geq 0$, and $u^2 + v^2 \leq 1$. Note that the surface element normal can be determined as[1]:

$$\boldsymbol{n} = \frac{\boldsymbol{s}}{\|\boldsymbol{s}\|}, \ \boldsymbol{s} \equiv (\boldsymbol{V_1} - \boldsymbol{V_0}) \times (\boldsymbol{V_2} - \boldsymbol{V_0})$$

As outlined by Möller and Trumbore, the intersection point can be uniquely found by equating eqs. (2.1) and (2.2) above:

$$\boldsymbol{O} + t\boldsymbol{D} = (1 - u - v)\boldsymbol{V}_0 + u\boldsymbol{V}_1 + v\boldsymbol{V}_2 \tag{2.3}$$

Rewriting and rearranging in terms of matrices gives

$$\begin{bmatrix} -\boldsymbol{D}, & \boldsymbol{V}_1 - \boldsymbol{V}_0, & \boldsymbol{V}_2 - \boldsymbol{V}_0 \end{bmatrix} \begin{bmatrix} t \\ u \\ v \end{bmatrix} = \boldsymbol{O} - \boldsymbol{V}_0 \tag{2.4}$$

Defining $\boldsymbol{L}_1 = \boldsymbol{V}_1 - \boldsymbol{V}_0$, $\boldsymbol{L}_2 = \boldsymbol{V}_2 - \boldsymbol{V}_0$, and $\boldsymbol{T} = \boldsymbol{O} - \boldsymbol{V}_0$, the solution can be obtained through Cramer's rule:

$$\begin{bmatrix} t \\ u \\ v \end{bmatrix} = \frac{1}{(\boldsymbol{D} \times \boldsymbol{L}_2) \cdot \boldsymbol{L}_2} \begin{bmatrix} (\boldsymbol{T} \times \boldsymbol{L}_1) \cdot \boldsymbol{L}_2 \\ (\boldsymbol{D} \times \boldsymbol{L}_2) \cdot \boldsymbol{T} \\ (\boldsymbol{T} \times \boldsymbol{L}_1) \cdot \boldsymbol{D} \end{bmatrix} \tag{2.5}$$

The algorithm must scan through all elements of the structure, following for each element the steps above in search for possible intersections. For large meshes, the computation can rapidly become prohibitive. For this reason, several checks are employed to quickly determine if an intersected point lies on a triangular element:

1. First, a back-face culling technique is applied so that if the normal of a triangular element is in the direction of an incoming ray, that element is ignored.

2. Second, if the ray is parallel to the plane of a triangle within an allowed tolerance, that element is ignored.

[1] Assuming that the vertices are given a counter-clockwise order as seen from a direction opposing the normal.

3. If the above two checks are satisfied, then a last check is made to determine the conditions for barycentric parameters u and v. If all conditions are satisfied, then the algorithm determines the intersection point within a triangular element.

4. Finally, a micro-architected surface may have many surface elements intersecting a given ray, but only the closest element is considered.

2.2 Generation of secondary rays

Once a collision is detected via the M-T procedure, the incidence angle of the primary ray on the selected surface element is determined as:

$$\alpha = \cos^{-1}\left(\frac{\boldsymbol{D}\cdot\boldsymbol{n}}{\|\boldsymbol{D}\|\ \|\boldsymbol{n}\|}\right)$$

Note that this angle of incidence is a local variable (given in a relative frame of reference). The pair (E, α) is then used to sample from bivariate relations giving, first, the number of secondary rays per incident primary ray [29]:

$$\gamma(E,\alpha) = 3.05 + 1.80\times10^{-5}\alpha^2 + 6.15\times10^{-7}E^2 - \frac{371.32 - \exp(0.05\alpha)}{87.60 + E} + \\ -1.97\times10^{-3}E - 0.11\cos(0.12 + 2.47\alpha) \tag{2.6}$$

Specifically, this function gives the SEE yield from a flat tungsten surface for a primary electron beam of energy E at an incident angle α. So once a collision has been confirmed, the function is evaluated with the primary ray's energy and angle of incidence and the resulting fractional yield is rounded up or down using a uniform random number generator[2]. This means that rays that produce yields $\gamma < 1$ may result in no secondary electron emission. If one secondary ray is emitted, the energy of the resulting electron is obtained by evaluating the accompanying function [29]:

$$E_{SEE}(E,\alpha) = 0.19E + 1.60\times10^{-4}E^2 + 0.15\alpha\sin(E) + 3.44\times10^{-15}E\alpha^7 - 6.54 \quad [eV] \tag{2.7}$$

[2]For example, if a yield $\gamma = 1.2$ is obtained, we sample uniformly in the interval $(0, 1]$ and if the random number $\xi_1 \geq 0.2$, then we round the yield down to $\gamma = 1$. Else, it is rounded up to 2.

Strictly speaking, expressions (2.6) and (2.7) are valid for $E > 100$ eV, but to capture rays with energies lower than 100 eV a smooth stitching of a polynomial function is performed. In the event that more than one secondary rays are produced, the energy of one of them is obtained as:

$$E_1 = E_{SEE}\sqrt{\xi_2}. \tag{2.8}$$

and emitted with an angle sampled from a cosine distribution:

$$\beta_1 = \sin^{-1}\left(\xi_2^{1/2}\right)$$

The second emitted ray then has an outgoing angle of

$$\beta_2 = \frac{\pi}{2} - \beta_1$$

and energy

$$E_2 = \cos^2\beta_1 E_{SEE}$$

If $E_1, E_2 < E_c$, the corresponding ray is terminated, where E_c is a threshold energy equal to $E_c = \Phi + E_f$ with Φ the material's workfunction and E_f the material's Fermi energy, 4.55 and 5.58 eV, respectively. [30, 31]. Therefore, once non-primary rays reach an energy less than the threshold, they no longer have the ability to emit secondary electrons.

The rays are tracked one at a time, from intersection to intersection until they terminate. Each primary ray creates a tree. For example, a primary ray that generates two secondary rays will add two branches to the tree.

$$\lambda_p \rightarrow \lambda'_d + \lambda''_d$$

$$\lambda_p\lambda'_d\lambda''_d$$

where the subindex d stands for 'daughter' ray. Once the calculations of a given branch are completed the algorithm moves to the next branch. If a given branch spawns another branch –third 'generation' (or gd, 'granddaughter') branch–, then it is added to the end of the tree and the tree moves on to next branch.

$$\lambda'_d \rightarrow \lambda'_{gd}$$

$$\lambda_p \lambda'_d \lambda''_d \lambda'_{gd}.$$

This sequence repeats until a tree has no further branches and encounters a null element. With this procedure, each ray's energy, angle, generation, and starting/termination point is tracked. Periodic boundary conditions are used along the x and y directions, while a flat boundary is used at $z = z_{min}$ to mimic a solid substrate beneath the foam. A ray (of any generation) that is found to reach z_{max} with an polar angle between $\pm\pi/2$ is considered and counted as a secondary electron emission event and a total escape from the foam.

This raytracing approach is trivially parallelizable, in the sense that each primary ray is independent and the geometry of the foam remains unaltered for all rays. This allows the method to run on multiple replicas and quickly generate large subsets of data, allowing the control of number of initial rays, energy, position and direction. The flow diagram of the entire process is given in Figure 2.1.

2.3 Finite element model and surface geometry development

The foam model is computationally reconstructed from a series of grayscale X-ray tomography images of a real foam with 65 pores per inch (PPI) and approximately 4% volume fraction V_f [32]. Each image is filtered and stacked to create a three-dimensional array with elements assigned either a value of 0 (space) or 1 (material). This voxel representation of the foam can be manipulated to change the foam's morphology, allowing for SEE yield comparisons to be drawn between foams of various porosities. The volume fraction of the foam is increased by adding layers of material voxels to the surface voxels, which are identified by their immediate proximity to voxels of value equal to zero. To prevent the growth of large, flat surfaces for the higher volume fraction foams which can adversely affect meshing quality, some randomness is included in the voxel layering process. This procedure is used to generate foams with V_f = 4%, 6%, 8% and 10%. Volume fractions are computationally determined by summing the material voxels and dividing by the total number of voxels in the domain. Although the procedure to generate these surfaces is general, this particular

structure is based on foams with pore and ligament sizes of approximately 270 and 80 μm, respectively [32].

An iso-surface routine is run on the voxel model to create the finite element model used for the raytracing study. The number of triangular surface elements generated is typically of order 10^7 and is reduced using a mesh coarsening routine to order 10^5. This ensures reasonable simulation runtimes and introduces a wider variety of element angles in the finalized mesh. An example of a finite element foam model is shown in Figure 2.2a. An important aspect of the mesh is the distribution of surface element normals that will be encountered by the simulated rays. Figure 2.2b shows a histogram of surface element normals for the geometry shown in Fig. 2.2a. As the figure reveals, the distribution of normals is not uniform, with a maximum observed for orientations near 90° (perpendicular to the z-axis). This is indicative of (nonuniform) pore shapes elongated along the vertical axis, a factor which will be invoked in Sec. 3.2 to explain some particular results.

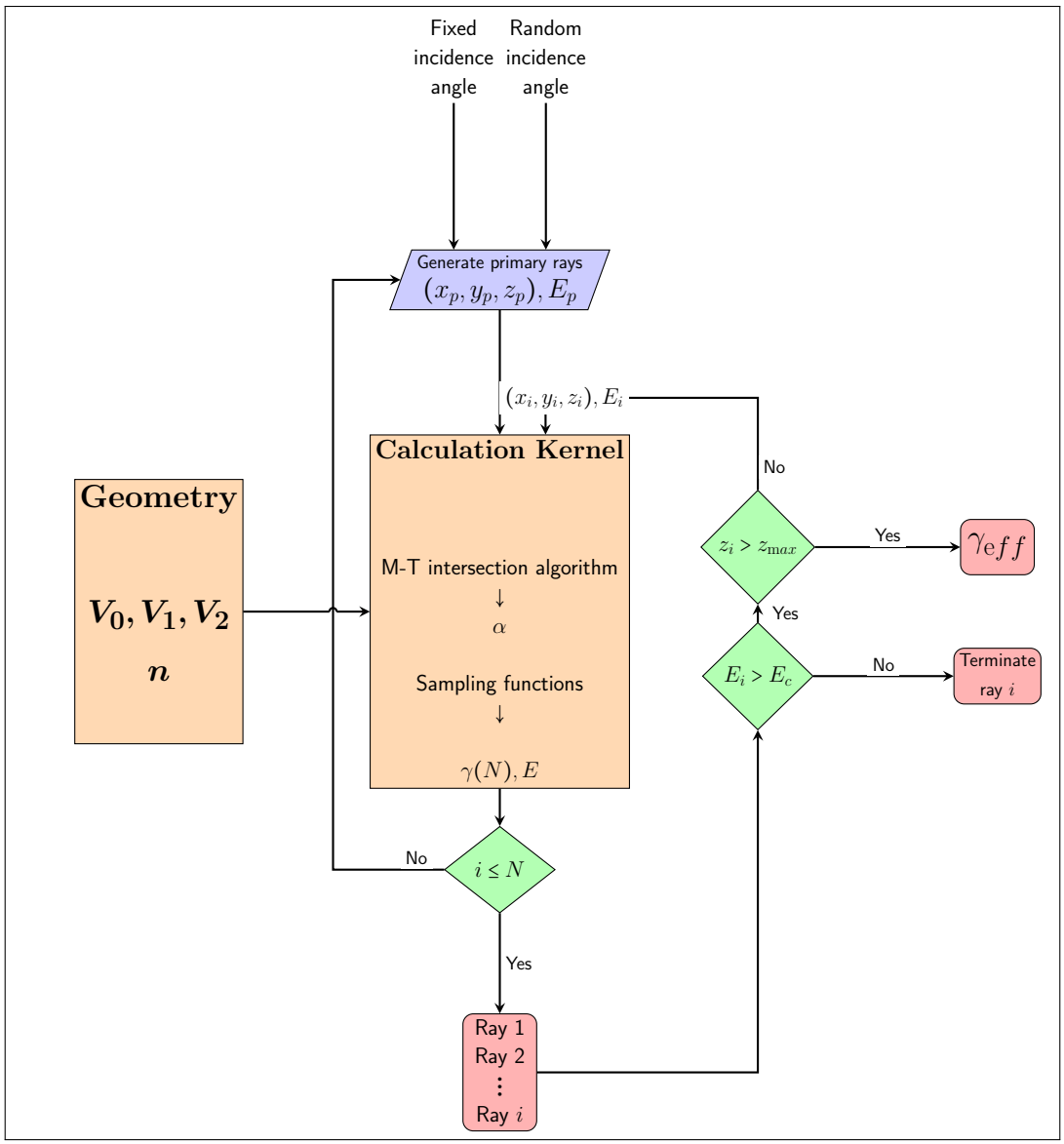

Figure 2.1: Flowchart of the raytracing Monte Carlo code.

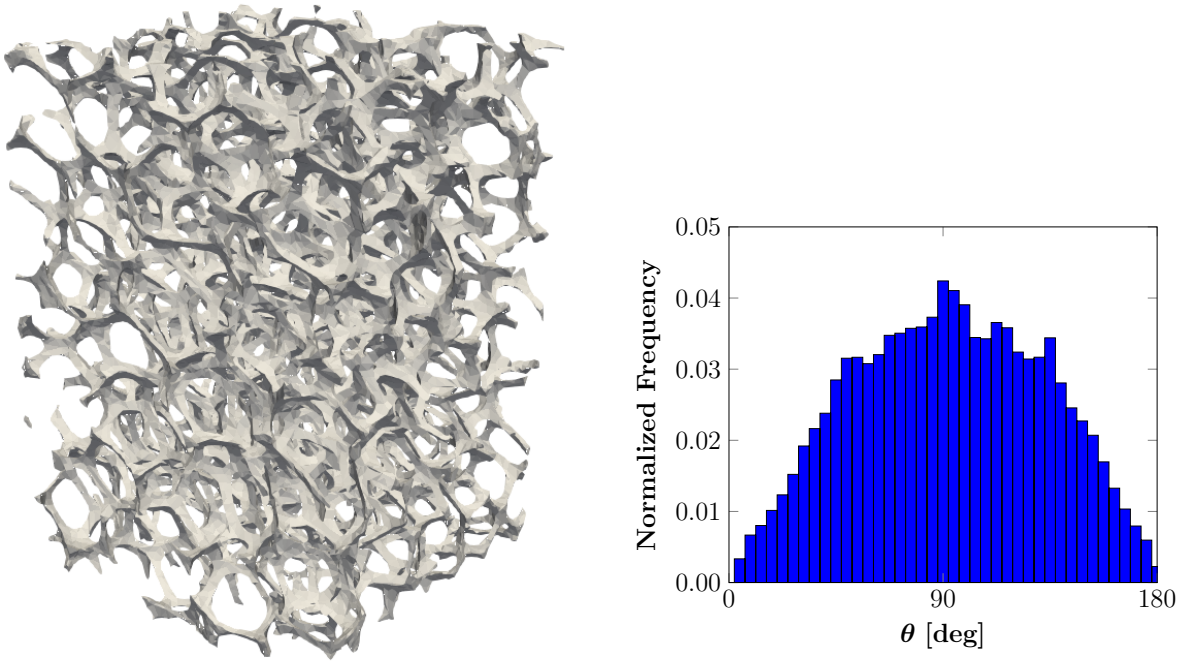

(a) (b)

Figure 2.2: (a) Finite element model of a real micro-architected foam structure rendered from X-ray tomography images. (b) Histogram of surface element normals.

CHAPTER 3

Secondary electron emission from a Raytracing Monte Carlo Model on Tungsten Foam

Several key results of the method are shown here. First, a series of verification tests to confirm the correctness of the implementation. Then the verified methodology is deployed to cases of practical interests such as the microfoam architected surface.

3.1 Verification

The first test performed involves studying flat W surfaces by sampling from the SEE yield surface as a function of incident energy and angle calculated in previous work [29] (eq. (2.6)). This simply verifies the implementation of the sampling procedure. The thickness of the sample is chosen so as to ensure that no primary ray has enough energy to traverse it up to 1000 eV. 10^5 rays per energy point are simulated, distributed over 10 computational cores. As Figure 3.1 shows the results using the raytracing method match exactly those given by the sampling function for normal incidence. The actual data from scattering Monte Carlo from which the sampling function is obtained is also shown for reference.

The second test is performed on an open cell (also known as 'open cage') structure, shown in Figure 3.2a, which is a simple way to represent foams with arbitrary porosity. It was proposed by Gibson and Ashby, who express the solid volume fraction of the structure as [33]:

$$v_f = \frac{\rho_c}{\rho} \approx C\left(\frac{t}{l}\right)^2 \tag{3.1}$$

where ρ_c is the relative density, ρ is the density of the material of which the cell is made, t

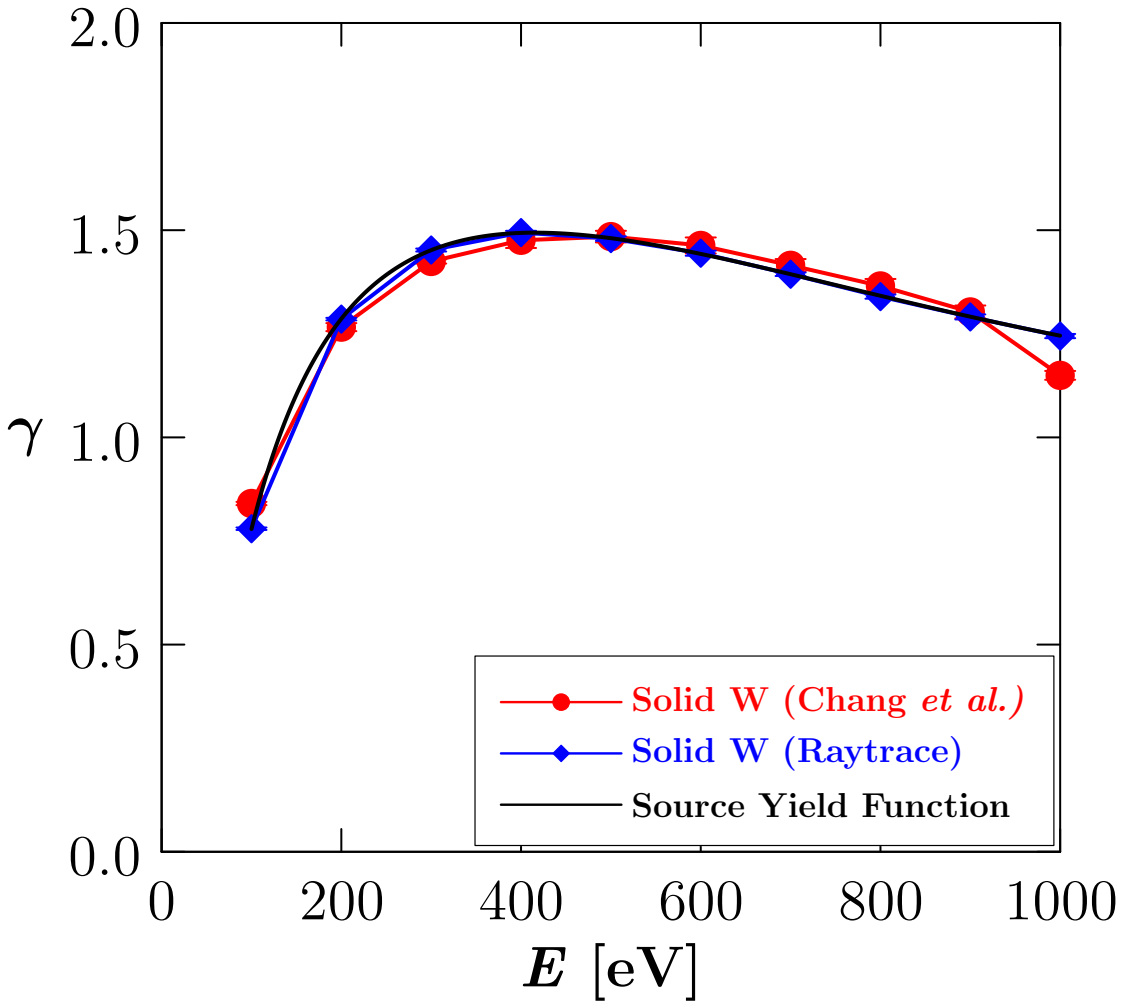

Figure 3.1: SEE yield as a function of primary energy for normal incidence on ideally flat W surfaces obtained using (i) scattering Monte Carlo (raw data from ref. [29]), (ii) sampling functions given in eq. (2.6), and (iii) using the raytracing model described here.

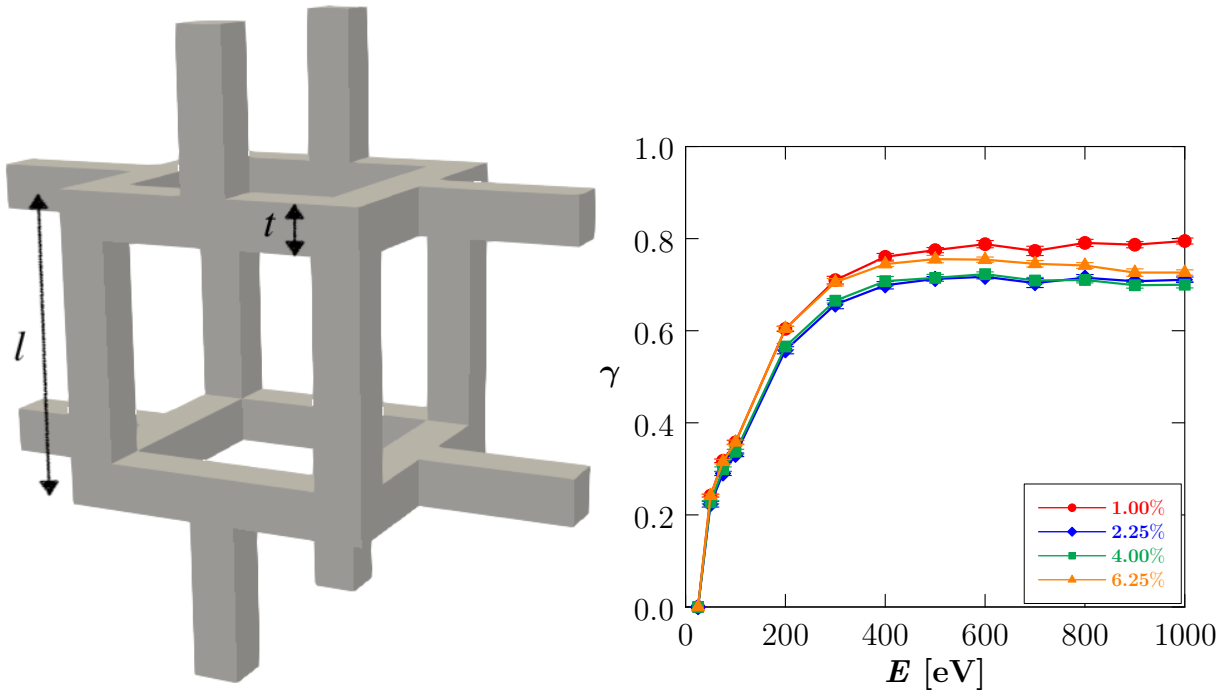

(a) (b)

Figure 3.2: (a) Image of a cubic open cell foam structure with the cage size l and ligament size t indicated. (b) Secondary electron yield versus electron beam energy at 0 degree incidence from the cubic cage.

is the ligament thickness, l is the cell size, and C is a proportionality constant with a value around 28. These cells can be used as repeat units of periodic arrangements simulating foams of arbitrary size. Next, the SEE yield for an open cage with volume fractions of 1.00, 2.25, 4.00, and 6.25% are calculated. A full-dense flat surface is assumed to lie beneath the cage, as to simulate an underlying solid substrate. The results are shown in Figure 3.2b for normal primary electron incidence. Interestingly, the maximum yield is obtained for the lowest volume fraction. This is an artifact due to the simulation setup, as in that case the ligaments are too thin to absorb any primary electrons and most of the primary rays hit the bottom substrate and secondary electrons are able to escape unimpeded.

3.2 Micro-Architectured Foam Structures

Four foam structures as the one shown in Figure 2.2a with varying volume fractions are are studied. Figure 3.3 shows the secondary electron emission yield for solid volume fractions of 4, 6, 8, and 10% in the 50-to-1000-eV energy range using normal incidence. The inset to the figure shows the dependence of the yield with the material volume fraction at energies of 50, 100, 200, 300, 400, 500, and 600 eV. In the high porosity range explored here the dependence of the SEE yield on V_f is clearly linear in the high porosity range explored here. For the sake of comparison, the maximum SEE yield for V_f = 4% (which occurs for E = 600 eV) is approximately 0.76, compared with a value of 1.49 for the flat surface (from Fig. 3.1). This decrease in SEE yield by about a factor of two is indicative of the potential performance gains that micro-architected surfaces might offer relative to fully dense surfaces. It is also worth noting that the results in Fig. 3.2b for an open cell cage with 4% material volume fraction is approximately 0.71, suggesting that such a simple model could be an acceptable surrogate for more complex geometries.

One issue that must be kept in mind when using material structures with finite characteristic lengths, such as the columns in the open-cell structure or the ligaments in the foam, is that electrons may be capable of traversing them in their entirety. Because our model only considers surface elements, this possibility is not captures in our calculations. In prior study

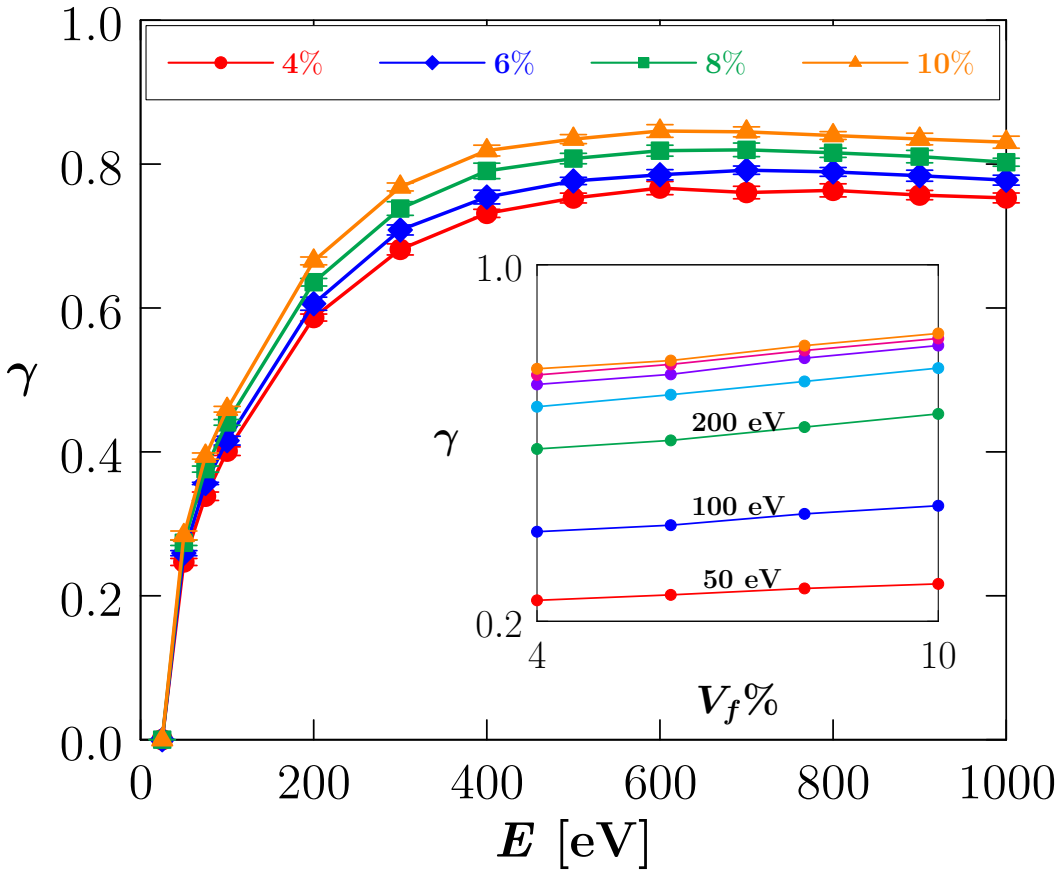

Figure 3.3: SEE yield versus electron beam energy initially projected from 0 degree incidence to the foam at varying volume-fraction percentages. The inset shows (in increasing order) the dependence of the yield with volume fraction for primary energies equal to 50, 100, 200, 300, 400, 500, and 600 eV.

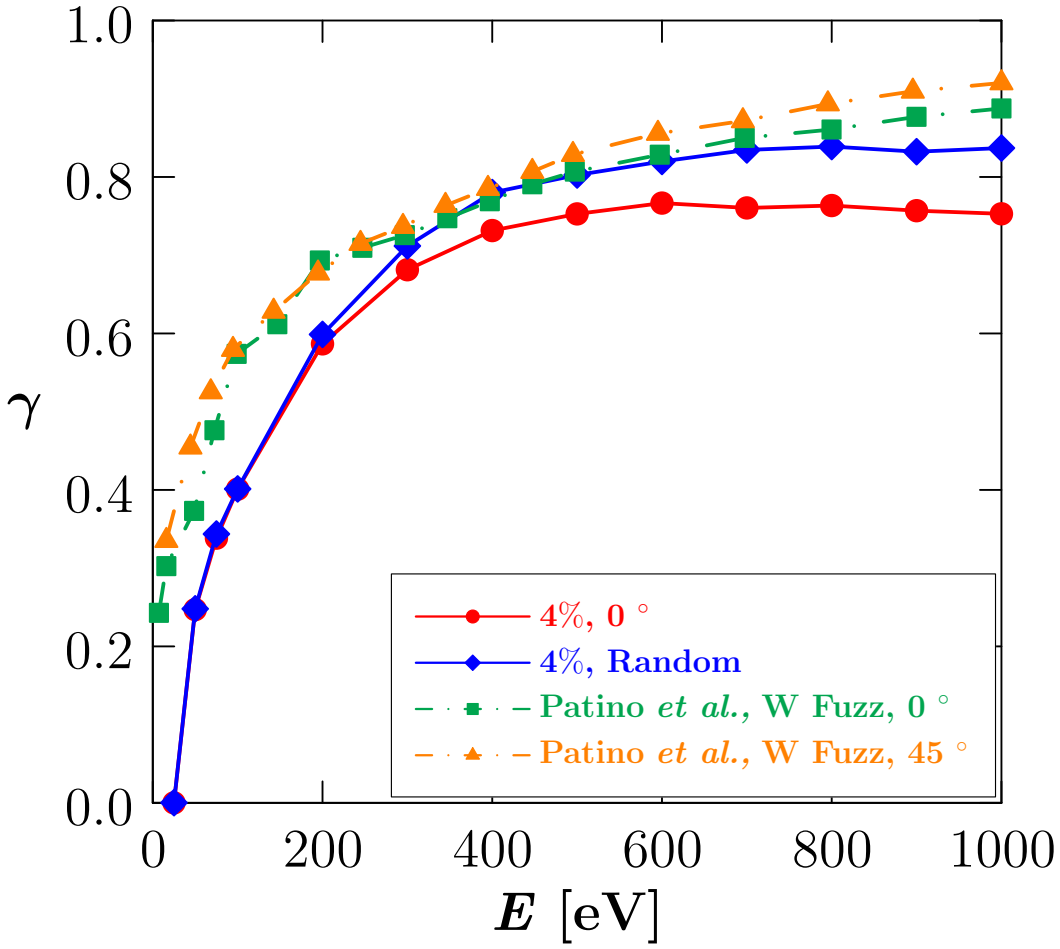

Figure 3.4: SEE yield versus electron beam energy for normal and random incidence primary electrons. Experimental results by Patino *et* al. [19] are shown for comparison.

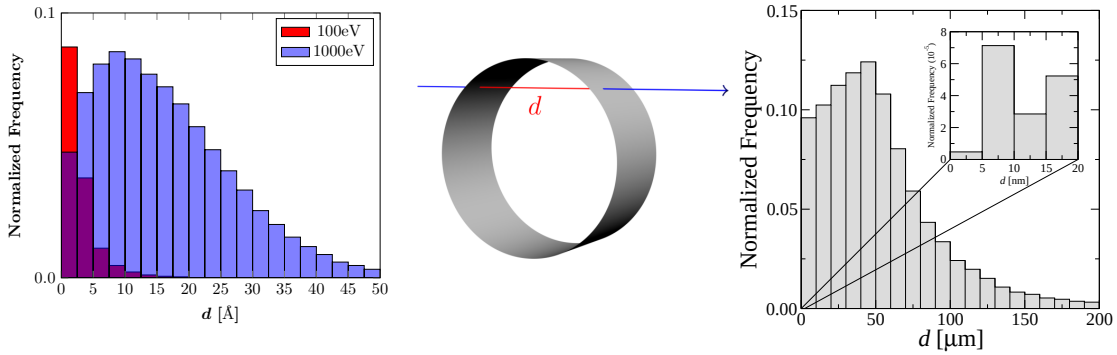

(a) (b) (c)

Figure 3.5: (a) Penetration depth distribution of thermalized electrons in bulk W with primary electron energies of 100 and 1000 eV at normal incidence. (b) Depiction of a possible ray trajectory through a ligament with d as the traversed distance inside it. (c) Distance d distribution of rays in a 4%-volume fraction foam surface.

[29], the absolute penetration depth of 100 eV electrons are calculated, which came out to be no more than 2 nm. These calculations are extended here to 1000-eV electrons, to have an upper bound in the absolute penetration depth. The result is shown in Figure 3.5a, where it can be seen that the tail of the depth distribution stops at approximately 5 nm. While this suggests that the effect can be neglected in our foam, with characteristic ligament diameters of 80 μm, a study is carried to estimate the relative occurrence of these events. The travel distance, d (shown schematically in 3.5b), are calculated for more than 200,000 random rays within the ligaments of the foam, and have integrated the relative frequency of having trajectories less than 5 nm. The results are shown in Figure 3.5c, with the inset showing an amplified view of the first 20 nm of the histogram. These results indicate that the probability of having rays that traverse ligaments over distances of 5 nm or less is approximately 10^{-5}. Since most of our simulations involve approximately 100,000 trajectories, this indicates that the model misses one ray in one hundred thousand, which can be considered negligible for all practical purposes.

Next to study is the effect of the incident angle on the results by carrying out a study considering random primary incidence vs. just normal incidence. Given that the distribution

of surface normals in the foam is not uniform (cf.— Fig. 2.2b), it is expected that there are some differences between both cases. As Figure 3.4 shows, these differences are more pronounced at high incident energies where primary rays with random incidence are able to impinge on high-angle surface elements at shallower depths and create more secondary electrons than normal rays, which are capable of penetrating deeper distances and become absorbed there. This is the reason behind the higher yields for random incidence shown in the figure. To confirm this, one can compute the penetration profile of the electron beam in both cases, obtained by tallying the depths at which electrons –regardless of what 'generation' they belong to– thermalize and become absorbed by the material. The results are shown in Figure 3.6, where it can be seen that, overall, normal-incidence rays penetrate further than the random incidence counterparts. The normalized depth can be scaled to typical foam thicknesses of approximately three millimeters, as described by Gao *et* al. [32].

Finally, the results are compared against experimental data. While no measurements have been made for W micro-foams, there are data available on He-plasma-exposed W surfaces [19], which are seen to develop a nano-tendril structure (commonly known as 'fuzz') at temperatures above approximately 900° [34]. These fuzz structures with characteristic ligament sizes of 10~20 nm resemble open foam surfaces with high porosity and can therefore be considered for comparison against our raytracing Monte Carlo calculations. The results are also shown in Fig. 3.4, where very good agreement is found between the calculations for the foam with V_f = 4% and the fuzz surfaces used in the experiments. The good match between the experimental data for 0 and 45° primary incidence serves as indirect indication that the distribution of surface normals in the fuzz is closer to uniform.

Next, we briefly turn back to the discussion in Chapter 3.2 on the effect of backscattered electrons (electrons that traverse an entire ligament) on the results of the model. In this case, the nanofuzz structure has comparable tendril sizes to that of the penetration depth of electrons. While discarding their contribution is not a concern for the foam (with ligament sizes of 80 microns), it could *a* priori result in a larger error in the calculations for the fuzz. However, there is another consideration to keep in mind here. Electrons become

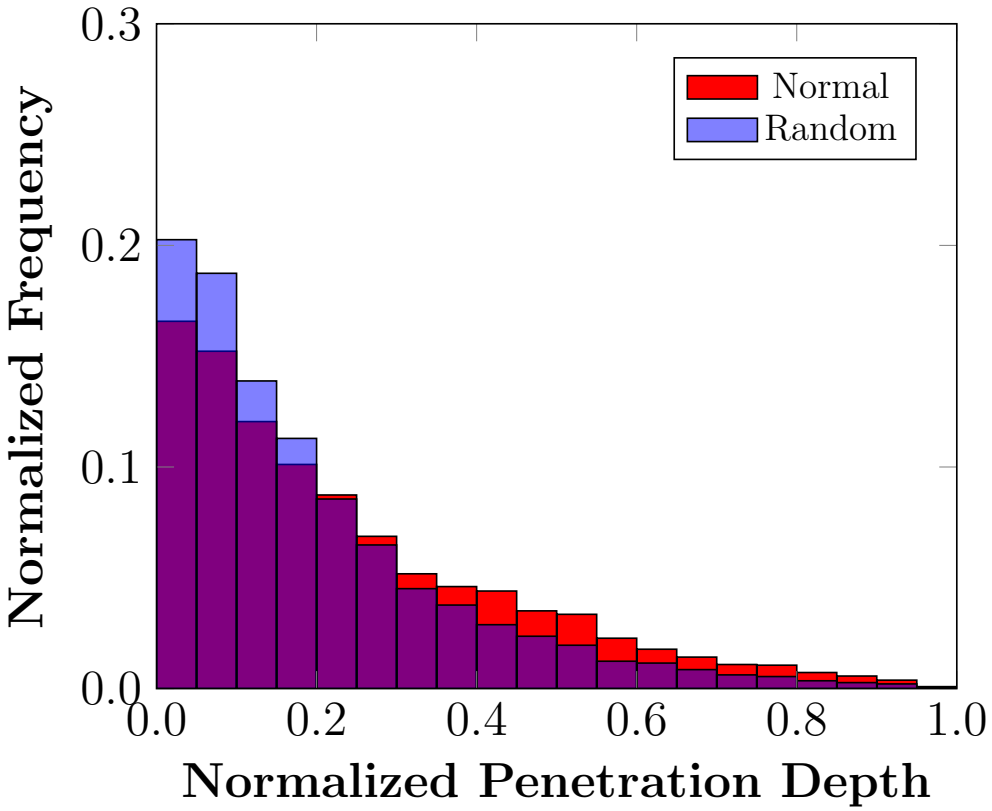

Figure 3.6: Penetration depth of electrons in a 4% volume fraction foam with an electron beam energy of 100 eV at normal and random primary electron incidence. This distribution corresponds to locations at which electrons 'thermalize' and become absorbed into the material. Typical foam thicknesses are approximately 3 mm [32].

'thermalized' within 5 nm of distance (in the most conservative scenario of 1000-eV primary energy). However, in the unlikely case that they traverse the entire tendril, their residual energy will be below the threshold to create further secondary electrons. Therefore, while it is acknowledged that this is missing in raytrace monte carlo model, there is confidence that it has little impact on the results shown here. Indeed, the fact that the model predictions produce such good agreement with the experimental measurements is an indirect indication of this.

CHAPTER 4

Conclusions of the Raytracing Monte Carlo Model on micro-architected surfaces for secondary electron calculation

Secondary electron emission is an important process in materials exposed to charged particle distributions (cf. Ch. 1). Measurements of SEE yields are challenging, and modeling and simulation can play an instrumental part in predicting the response of complex surfaces to electron exposure. Models can also be used as a way to pre-assess the suitability of a specific surface morphology prior to developing costly fabrication techniques [35, 36, 37]. For this, computational methods must display sufficient efficiency to parse through the parametric space, which can be large if one takes into account the multiple length scales of the problem, such as pore size, ligament size, total thickness, total exposed area, etc. Developed here is an experimentally-validated methodology that simulates electron irradiation on a surface using rays generated randomly with a given set of properties. This technique, known as 'raytracing' Monte Carlo, is routinely used in the visual graphics industry to create shades and lighting effects [38, 39, 40]. The interaction of each ray with the surface consists of a mathematical determination of the possible intersections with it, and a physical description of an incident ray impinging on a surface. Per se, our model is trivially-scalable and can run on multiple processors without any communication cost.

However, to be fully applicable, the methods proposed for this model must satisfy three premises:

1. That a surface structure with arbitrary geometric complexity can be reduced by dis-

cretization to a piecewise collection of flat surface elements on which to apply the secondary electron physics of flat surfaces.

2. That electron irradiation on these discretized geometries can be effectively simulated with individual rays representing electron trajectories.

3. That the typical ligament size always be much larger than the electron penetration in the material at all energies considered. In this sense, the raytracing approach proposed here is not conceptually too different from the original neutron transport Monte Carlo methods developed several decades ago to study neutronics in nuclear reactors [41, 42].

The M-T algorithm acts as the bridge between the discretized material surface and the raytracing approach. A feature not to be overlooked is the pre-computation of SEE yields and energy distributions for flat (ideal) surfaces. It is in these calculations where all the physics around electron-matter interactions is contained, such that the problem of SEE from complex surfaces can be easily separated into a 'physics' part (in idealized scenarios) and a 'geometry' part (discretized to take advantage of the physical calculations). This division affords a great deal of versatility, so that as long as a sufficiently fine mesh can be generated one can conceivably study geometric features as fine as nanopillars, internal voids, surface islands, or even asperities associated with surface roughness.

This is the case in this work, where porous foams with volume fractions $< 10\%$ have been studied. Foams of this type, with thicknesses as thin as just a few microns lying on solid substrates are shown to reduce the SEE yield by over 50%. This is an encouraging finding to promote the use of these micro-architected structures in materials exposed to charged plasmas. Work to extend this methodology to dielectric materials of interest in plasma thrusters for electric propulsion (BN [43, 44, 45, 46]) is currently underway[47].

While the present model ignores backscattered electrons, shown here with confidence is that their effect is negligible for the systems considered in this paper. There are computer codes that do capture this contribution, chief among which is `Geant4` [48, 49], although they are somewhat less adaptable to complex geometries such as the one considered here. Another

aspect worth mentioning is the fact that porous materials have traditionally been used to enhance SEE, not lessen it as is the case here. However, secondary electron multiplication is usually accomplished under a high voltage condition, with energies much higher than those employed in this work. As well, the typical Debye length (on the order of 10^{-4} m) of plasma devices of interest is larger than the surface architecture characteristic length scale (on the order of tens of microns), and it is therefore safe to neglect the electric and magnetic fields when tracking the trajectories of electrons. This is showcased in studies with textured surfaces, e.g. as in refs. [50, 18].

Finalizing the discussion of the RTMC model is the computational cost of the calculations in Figure 4.1. The figure shows the CPU time per primary ray monotonically increasing with primary energy for normal incidence in the foam with 4% porosity. The explanation for this increase lies in the number of branches (rays) created by each primary ray, which depends on the SEE yield at each energy. This is shown in red in the plot (vertical scale shown on the right). The curves suggest that a representative CPU cost per ray is approximately 0.035 seconds[1].

To summarize the last 4 chapters and the Raytrace Monte Carlo model:

1. A raytracing Monte Carlo approach is made that generates random electron trajectories and determines their intersection with solid surfaces via the Möller-Trombore algorithm.

2. Each intersection is characterized by an impinging angle and energy, from which partial electron emission trajectories can be generated from pre-calculated relations.

3. All trajectories are tracked until either an electron emission is recorded or until the energy of the ray falls below the threshold energy for escape.

4. Microfoams with 96 to 90% porosity reduce the net SEE yield by approximately 50% in W surfaces.

[1]This is for Intel Xeon E5-2650v4 CPUs installed on the `hoffman2` cluster at UCLA, running at 2.2 GHz, with 4 GB of memory.

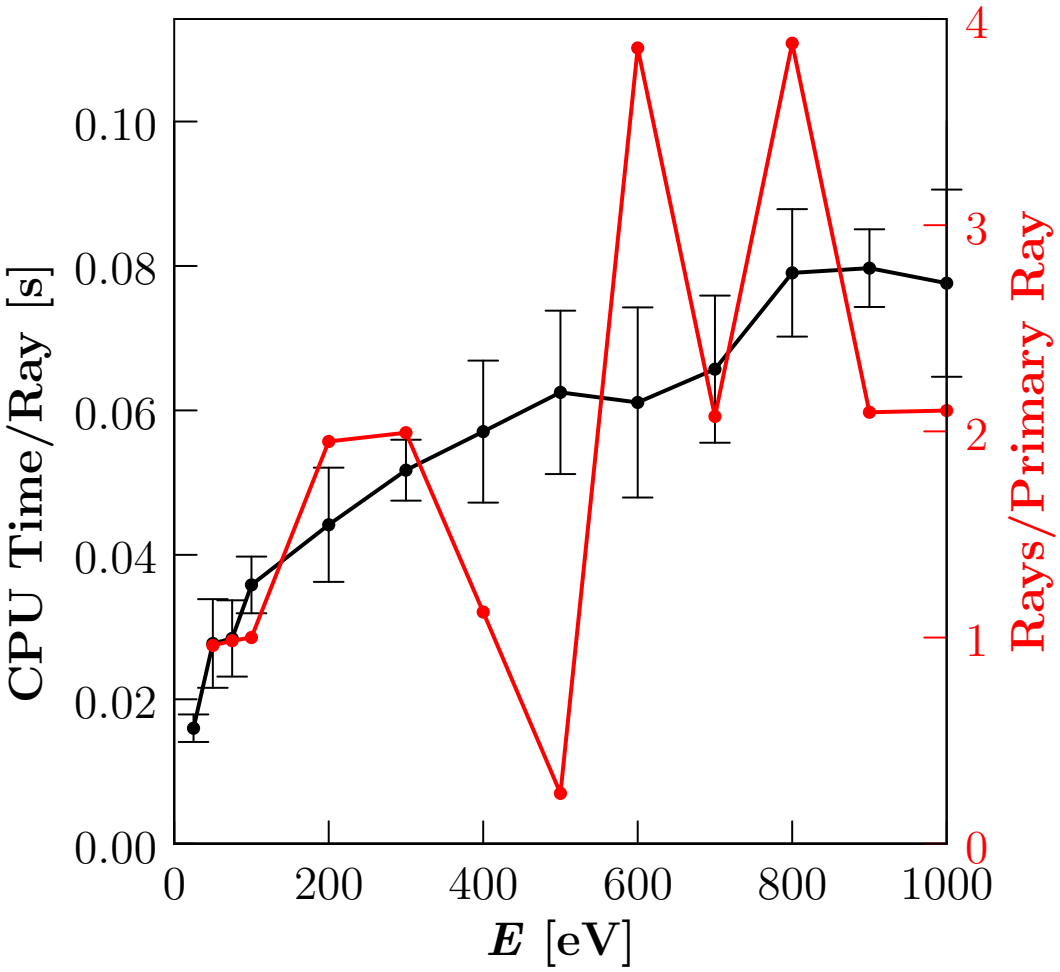

Figure 4.1: Computational cost (measured as CPU time) per primary ray as a function of primary energy. The CPU overhead loosely correlates with the number of daughter/granddaughter rays generated by each primary ray (in red).

5. Very good agreement between the full approach and measurements of SEE yields in W-fuzz surfaces across a wide energy range.

CHAPTER 5

Sputtering Effects on Micro-Architected Surfaces

In electronic devices like ion thruster and hall thrusters, the effects from the present plasma can devastate the structural integrity. In general, plasma devices suffer degradation from sputter and erosion effects[51, 52]. In order to estimate a thruster or spacecraft component a vast range of experimental procedures are to be followed. Even if the effort is put into evaluating the lifetime of a component the estimation of thruster and spacecraft component lifetime is fraught with relatively high uncertainties. A typical approach for evaluation is to model an in-space plume profile and then assess the resulting erosion rate from the material sputter yield based on the plume properties at the plume-surface interface. One may imagine, ignoring the uncertainties in the projected plume properties at high angles from the thrust axis for the moment, presents several challenges. To this extent the available sputter yield data for various materials tend to be rather sparse, and extrapolation to the range of interest can add to the high error. For regions where sputter yield data are available, there can be high uncertainties and conflicting results from different laboratories. Finally, if the measurement data can be assumed to be precise and accurate, there are uncertainties in translating the yield results from laboratory conditions to actual in-space conditions.

For most state-of-the-art EP devices, namely gridded ion engines and Hall effect thrusters, the propellant of interest is xenon gas, and for regions of the plume where impingement is likely to occur, the ion energies are relatively low, on the order of hundreds of eV or less [52]. For the reasons expressed above, availability of data in these ranges, for the materials of interest to spacecraft interaction, are limited. Therefore, there is a need for a measured approach in evaluating the available data for application to spacecraft erosion from EP plumes. Currently, there are few models to simulate the growth or deterioration of a material

due to sputtering effects. Often these models rely on a viewing factor, where surfaces are given a weighted scale of erosion rate or deposition rate based on how exposed they are with respect to a point of view [53].

Here, the raytrace Monte Carlo method of tracking particles is developed so that the sputtering yield of a material is calculated, and the morphology of the material is adaptively evolved using an evolutionary algorithm.

CHAPTER 6

Sputtering Yield using Raytrace Monte Carlo method and Adaptive Meshing for Evolving Surfaces

Following the model discussed in Chapter 2.1, the only deviation to the raytrace Monte Carlo model itself is within the bivariate sampling functions. It has been expressed that one of the advantages to the RTMC model is the distinct independence from geometry of the structure and the physics of particle transport. With the sampling functions holding the physics, here the focus will be on extending the model to encompass sputtering effects by using an adaptive meshing approach. Here, the model is developed for Xe+ ions impinging on the same tungsten foam used in earlier chapters.

6.1 Bivariate sampling functions

There are numerous theoretical models that handle the deposition and sputtering of impinging particles. Here, the main software used to create the bivariate sampling functions comes from TRIM (the TRansport of Ions in Matter). This comprehensive program is included within the scientific software package SRIM (the Stopping and Range of Ions in Matter), a work distributed by IBM-Research [54].

SRIM is based on a quantum mechanical treatment of ion-atom collisions. The stopping and range of ions are calculated within the energy of 10eV to 2 GeV, well within the necessary range for this study, approximately 300 eV. For the particular purpose of calculating surface sputtering with TRIM, three material input parameters are of importance: the lattice displacement, surface binding and lattice binding energies. In the present calculation,

the lattice displacement energy, surface binding and lattice binding energies are chosen as 25, 8.68 and 3 eV, respectively, as suggested by the TRIM table. Given that the sputtering yield is most sensitive to the surface binding energy, the surface binding energy can be treated as a calibration variable.

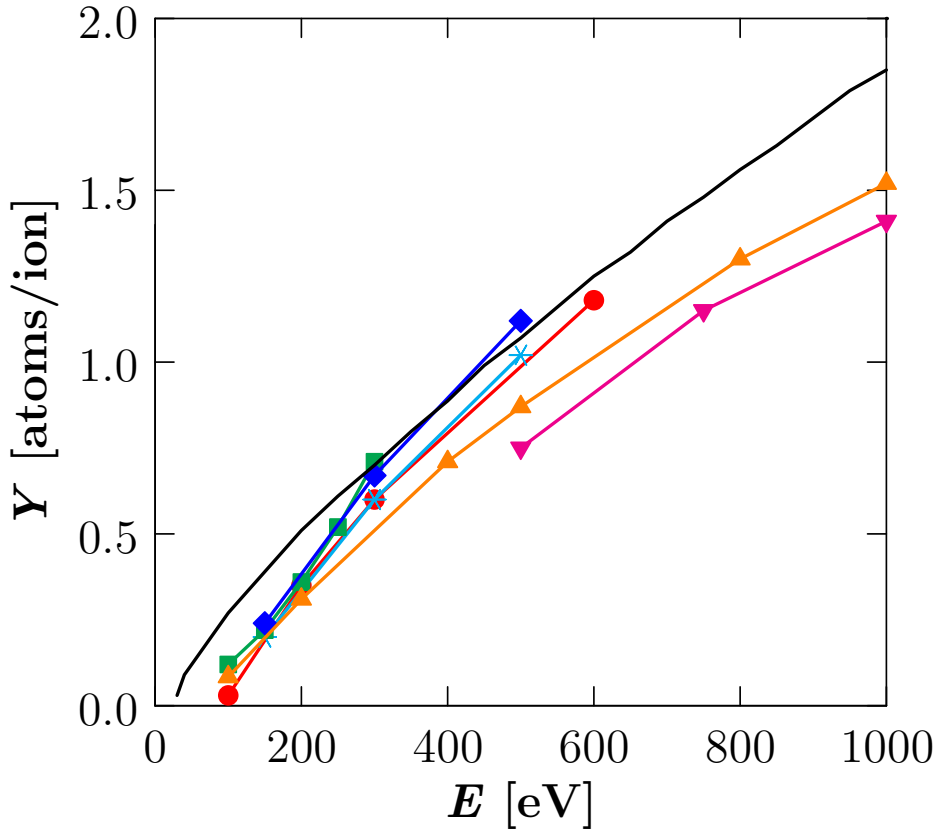

Figure 6.1: Total sputtering yield from smooth W surface as a function of primary electron energy for electrons incident at 0°. • = Rosenberg (1962); ∗ = Wehner (1962); ■ = Stuart (1962); ♦ = Winters (1974); ▲ = Doerner (2005); ▼ = Tartz (2011); solid line = TRIM. [55, 56, 57, 58, 59]

The raw data shown in 6.1 is fit to a bivariate mathematical function using *symbolic regression* (SR) through genetic evolutionary algorithms for machine learning [60]. The final

expressions for the total sputtering yield and energy distributions are:

$$Y(E,\alpha) = 7.246\times10^{-2} + 2.236\times10^{-3}E + 4.875\times10^{-5}\alpha^2 + 4.775\times10^{-7}E\alpha^2 - 5.515\times10^{-3}\alpha - 4.702\times10^{-7}E^2 - 6.214\times10^{-11}E\alpha^4 \tag{6.1}$$

$$E_{out}(E,\alpha) = 31.38 + 1.812\times10^{-2}E - 569.7/E + 2.789\times10^{-3}\alpha^2 + 9.318\times10^{-8}E\alpha^3 - 0.1\alpha - 2.533\times10^{-7}\alpha E^2 \tag{6.2}$$

6.2 Adaptive Meshing Approach

6.2.1 Mesh Evolution

In the RTMC model, all rays are tracked from initiation up to termination. The termination point of a ray can be counted toward a deposition if it is on face element. However, if a ray's initiation begins at a face element and does not terminate at an element than the initial element would have a net sputtered yield. With this a method of bookkeeping the net loss or gain on an element can be made. Suppose a mesh of surfaces modeled in finite-element

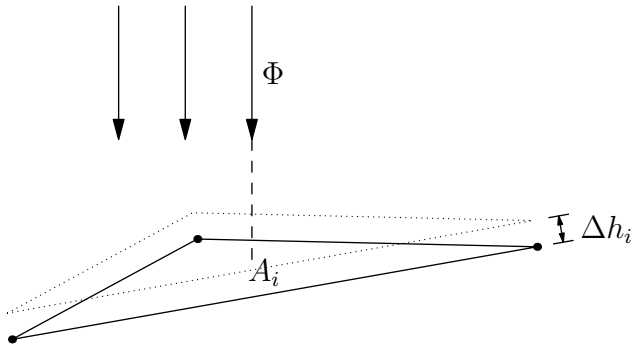

Figure 6.2: Depiction of an effective flux and net yield on a triangular element i

fashion as discrete triangular elements joined at the vertices (nodes). An exposed surface area A is vulnerable to impinging ions from above. The rate of impinging ions is the ion flux ϕ, the rate of transfer of ions through an area:

$$\phi = \frac{\#\text{ of ions}}{A\cdot\delta t}.$$

While the number of ions pass that pass through i^{th} surface element per unit time is

$$\phi_i = \phi A_i.$$

From the flux a timestep can be conceived. If the flux is given, the area of the structure is known, and the number of rays thrown on the mesh is a user input then the timestep for N total rays is:

$$\delta t = \frac{N}{A\phi} \tag{6.3}$$

Additionally, the RTMC model tracks the number of particles coming in N_i^{in} and out N_i^{out} of the triangular element i. Then a net sputtering yield γ_i^{net}, the number of atoms ejected from the target per incident ion, can then be calculated as

$$\gamma_i^{net} = N_i^{out} - N_i^{in}$$

The growth ($\gamma_i^{net} < 0$) or lowering ($\gamma_i^{net} > 0$) rate $v = \Delta h/\Delta t$ can be calculated as

$$\frac{\Delta h}{\Delta t} = \frac{\gamma_i^{net}\Omega\phi A}{A_i N_i^{in}} \tag{6.4}$$

where Ω is atomic volume. Assuming the growth or decrease occurs with respect to the normal of the triangular element, the evolutionary algorithm for each element is:

$$h_i^{n+1} = h_i^n + \frac{\gamma_i^{net}\Omega\phi A}{A_i N_i^{in}}\Delta t \tag{6.5}$$

As displayed in figure 6.2, an individual element would then grow or decrease with respect to the yield and the normal of the triangular plane.

6.2.2 Laplacian smoothing

Once all elements have the evolutionary algorithm applied the set of discrete triangular elements, or mesh, must be updated so that minimal defects arise. The disconnect of nodes from shared faces are among the obvious defects to manifest. A smoothing technique is necessary to recombine nodes and vertices. Laplacian smoothing is by far the most common smoothing technique. In its simplest from, this smoothing consists of recursively placing

each node at the average of the nodes connected to it. In a mathematical expression:

$$x = \frac{1}{m} \sum_{i=1}^{m} x_i \tag{6.6}$$

where x is a specific node and m is the total number of faces that explicitly share that node. Therefore, it is more likely that a set of faces will be displaced rather than one individual face per timestep. Figure 6.3 shows the steps involved in remeshing, the bottom left panel is directly after Laplacian smoothing. In this step an attempt to make the mesh watertight again is made.

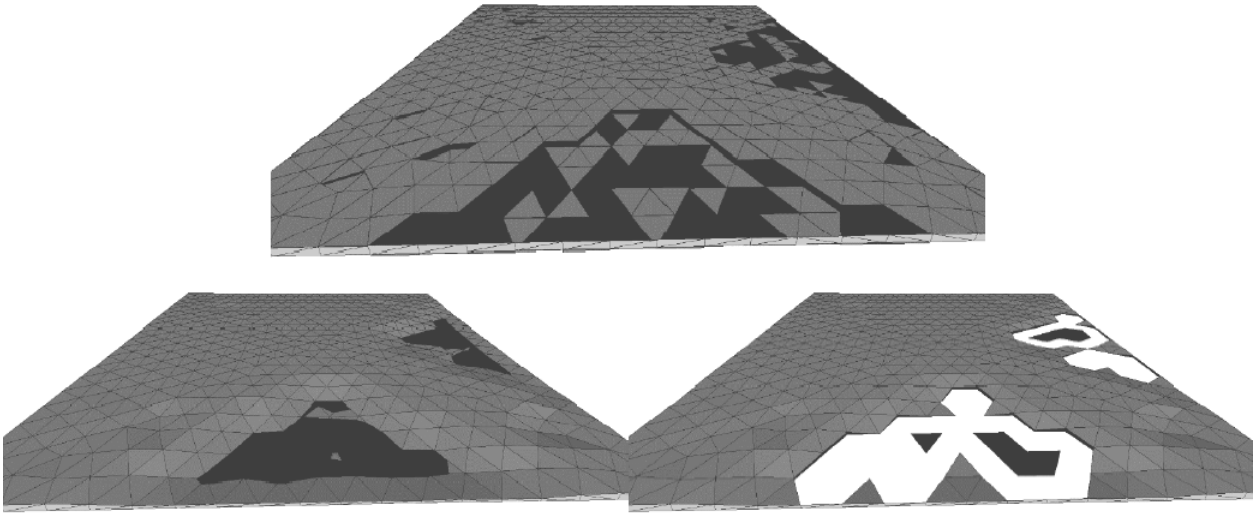

Figure 6.3: Adaptive meshing of a simulated flat W surface. Top: After evolution algorithm. Bottom left: Laplacian smoothing. Bottom right: Intersection removal.

6.2.3 Self-intersection Detection and Removal

Another issue that may manifest after applying the evolutionary algorithm is the creation of self-intersecting elements. Even after applying a Laplacian smoothing, it may be that two elements are intersecting as shown in the bottom left panel in figure 6.3 and figure 6.4. There are numerous libraries and techniques for detecting and eradicating these self-intersections. Employed here is a self-intersection detection library created by Devillers and Philippe [61].

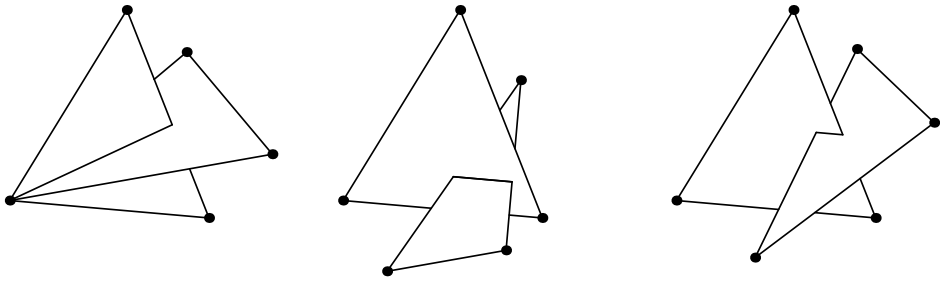

Figure 6.4: Several depictions of self-intersecting triangular elements.

The probability of a self-intersection to occur within one timestep is governed by the Courant Friedrichs Lewy condition. In the case for foam structures, the rate of growth or decrease must not exceed the thickness of a ligament l for several timesteps or iterations. This condition corresponds to

$$\frac{C\Delta h}{\Delta t} \cdot t_{tot} \leq l$$

with C as a scalability factor and t_{tot} is the total run time. Once this this criterion is met a remeshing of the structure must be made. Software such as Meshlab [62] offers floating island removal or hole patching capabilities to facilitate remeshing the structure once ligaments are breached. A flowchart of the extent of adaptive meshing RTMC is shown in figure 6.5.

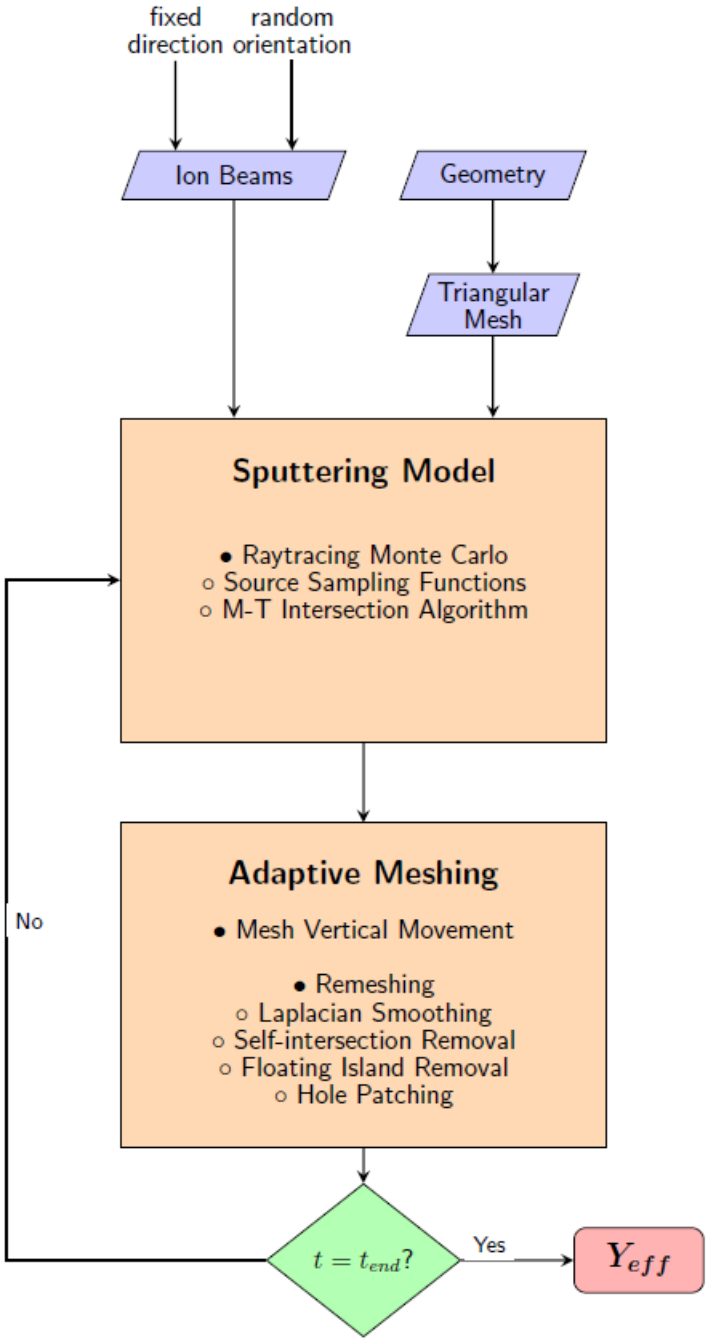

Figure 6.5: flowchart of the adaptive meshing RTMC.

CHAPTER 7

Sputtering effects from Raytracing Monte Carlo Model on Tungsten Foam

Here, bulk W and a foam W are under Xe+ irradiation at 300 eV. A flux of $1 \cdot 10^{13}$ ions/mm^3 is used. A scaling factor of 100,000 is used to increase the number of rays per iteration to 10^{11} rays. The scaling factor is within the Courant condition such that the ligaments of the foam $80\mu m$ is much larger than the change in height with respect to a face's normal. Remeshing occurs after every iteration, with timesteps at approximately $\delta t = 0.025s$. To the authors knowledge there is currently no experimental data nor theoretical data pertaining to Xe+ irradiating a 4% V-F foam at 300 eV. Therefore, the following results must be taken as a feat to capability rather than physical accuracy.

Figure 7.1 compares a W bulk block against 4% V-F W foam. From the results of adaptive meshing RTMC, figure 7.1 shows a noticeable decrease in the total escaped sputtered atoms between bulk and foam. As shown in the chapters pertaining to SEE, again the reduction in sputter yield for Xe+ impinging on W is reduced by roughly 50%. As time increases, both the W bulk and W foam sputtering yields decrease. Additionally, note in figure 7.1 that the drop in the yield for foam is larger than the bulk within the range of 20 seconds. It is possible there is a dip in the yield before increasing the yield as time increases. The foam could be losing volume such that the yield is lower for a range of lower volume fraction foams. This event is shown in the SEE results of figure 3.2b and 3.3.

The termination of rays is tracked within the 4% V-F foam such that a frequency of terminated rays is compared at different set depth of the foam. In figure 7.2, the top of the foam is at $z = 0.0$ while the bottom of the foam is at $z = 1.0$. Figure 7.2 reveals that as time

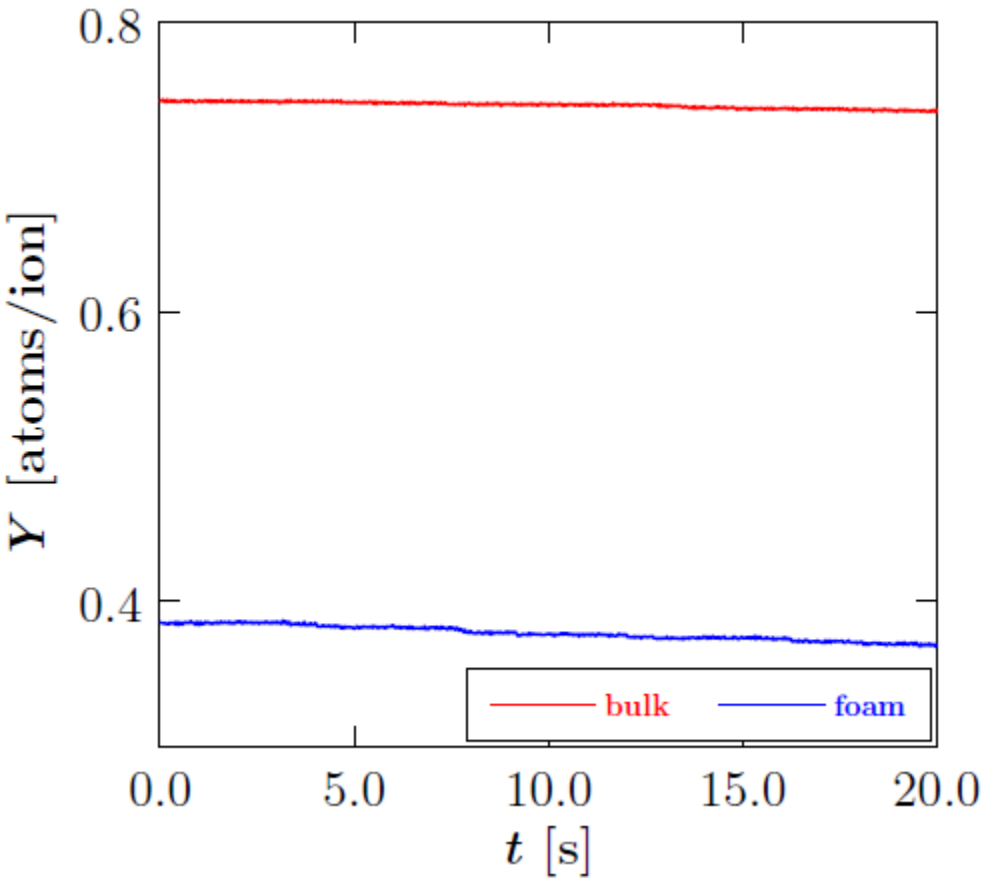

Figure 7.1: sputtering yield versus time

increases the number of rays terminated near $z = 0.0$ decreases. This suggests a decrease in volume at the top of the foam, or a shrink in elevation near at the very top of the foam. At later times the mid-range depth encounters a larger count in terminated rays. This suggests that either indeed the top layer is losing volume, or the middle of the foam is gaining volume. To capture how the particles may be redistributed within the foam a test on the ligament thicknesses at set depths is fashioned.

Using the same set of depths as in figure 7.2, rays are used to intersect ligaments and determine ligament thickness. The back-face culling effect in the raytrace algorithm is reversed so that rays only traverse inside a ligament. The distance traversed within ligaments are calculated and averaged at varying depths. Figures 7.3 and 7.4 portray the average ligament thickness at the given depths throughout the foam. Although a curve for $z = 0.0$ would have

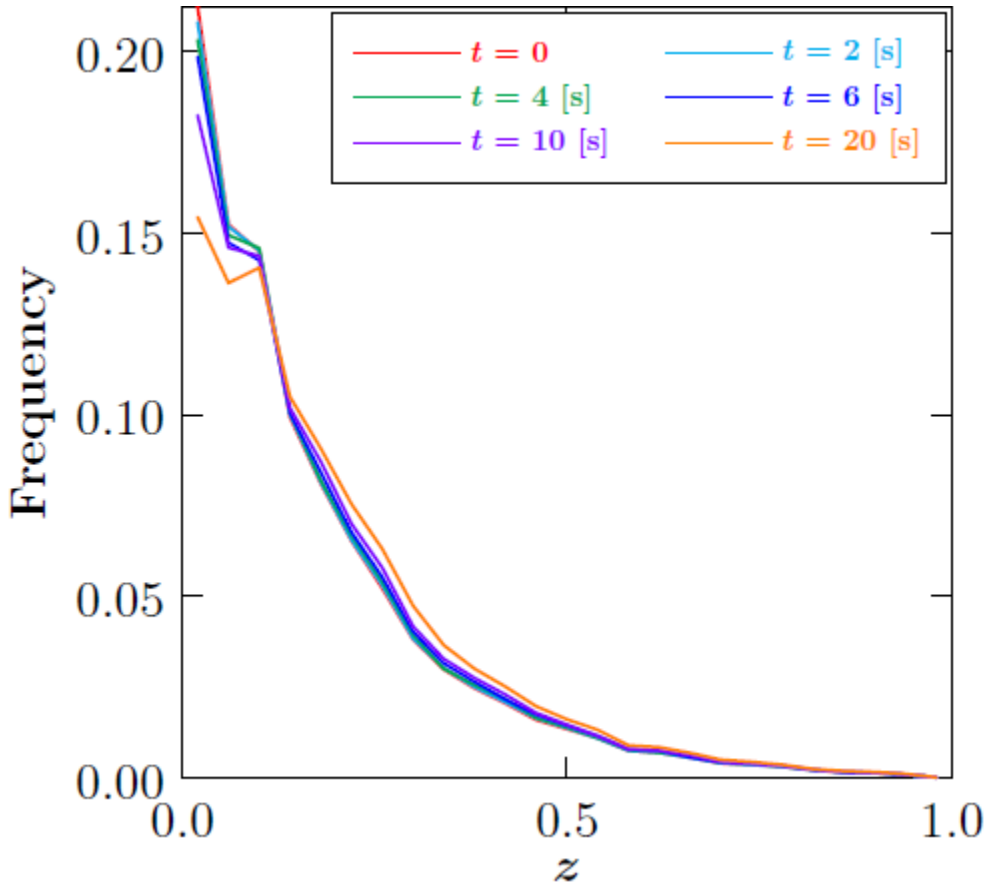

Figure 7.2: Normalized penetration depth frequency count for t = 0, 2, 4, 6, 10, 20 seconds.

been appreciated, it is found that after the test the foam's height is decreased. Therefore, values for the ligament thicknesses are not found at $z = 0.0$ after several iterations. Instead, shown in figure 7.3 and 7.4 are the ligament thickness and percentage change at 10, 30, 50, 70, and 90% into the foam. From figure 7.4 the curves beyond 50%, or the bottom half of the foam show an increase in ligament thickness, while the top half has a general decrease suggesting a redistribution of volume within the foam. The top loses volume while the bottom half gains.

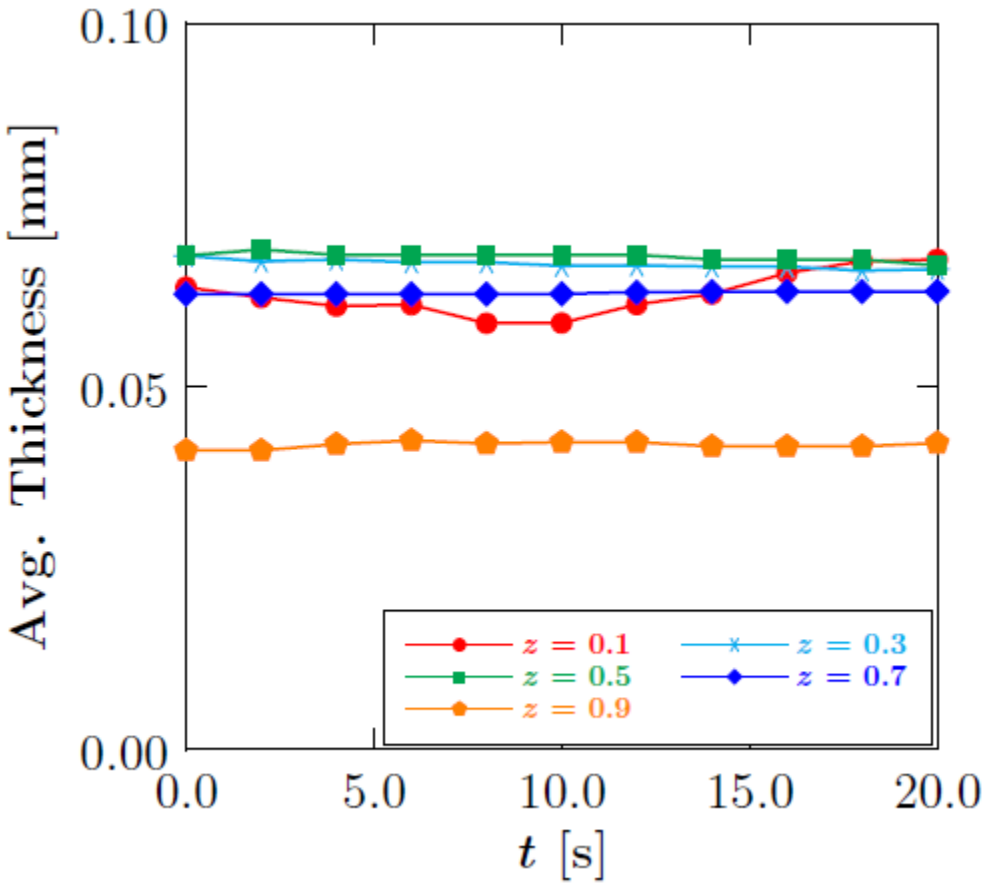

Figure 7.3: Average ligament thickness vs. time for normalized depth z = 0.1, 0.3, 0.5, 0.7, 0.9.

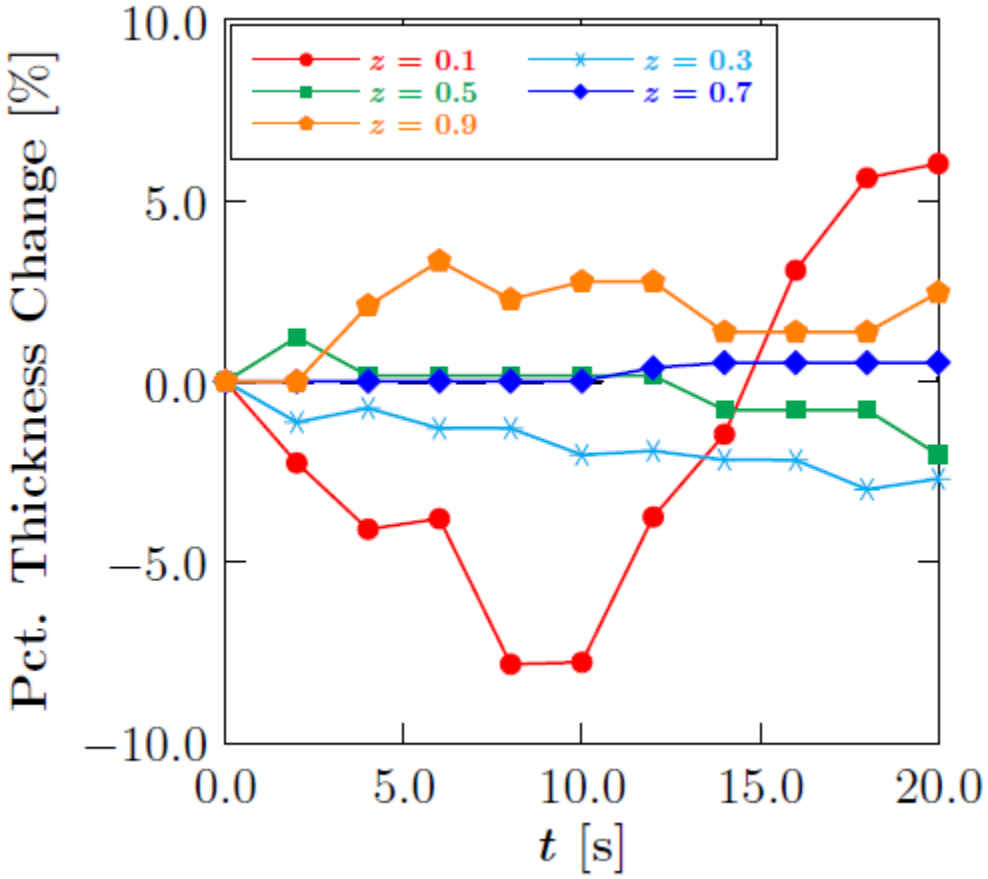

Figure 7.4: Percentage of ligament thickness change vs. time for normalized depth z = 0.1, 0.3, 0.5, 0.7, 0.9.

CHAPTER 8

Conclusions of the Adaptive Meshing Raytrace Monte Carlo Model

Ion bombardment on metals such as tungsten can have devastating effects for component integrity. The cost and challenge of experimentally surveying several materials, beyond the mention of micro-architected surfaces, significantly delays the discovery and invention of effective components for plasma facing device use. Shown here is the morphology of a W foam significantly reducing the sputtering yield when compared to a bulk structure. The yield decreasing by roughly 50% may remarkably improve conditions for plasma interacting materials. Additionally, shown is a redistribution of particle matter within the foam, suggesting a notable healing factor. A reduction of the sputtering yield not only improves the integrity of the components but also the plasma itself by reducing dust pollutants [63].

Here, a model is produced to study complex geometry irradiated by ions. Although a single demonstration on a 4% volume fraction foam is tested, the geometry, chemical species, and sizes are all easily swapped. This model can be used to generate optimal surfaces prior to costly development, trial and error, and any real exposure. This raytracing Monte Carlo technique has been adapted to suit sputtering effects with relatively no change to the overall model. The RTMC model has been tested rigorously by way of secondary electron emissions and expanded to include sputtering effects. This technique encompasses the issues related to pore size, ligament size, exposure area, and porosity. Due to the versatility of the RTMC technique, continued development of the model can prove to efficiently surmise the stages and morphological change of plasma facing designs.

To summarize the last 4 chapters of the adaptive meshing Raytrace Monte Carlo model:

1. The same raytracing Monte Carlo approach used for calculating SEE is adapted so that time dependence of the sputtering yield is manifested.

2. Not only is each intersection characterized by an impinging angle and energy but also each triangular element is characterized by an effective flux, from which a height change with respect to a face normal is made.

3. The morphology of the foam is evolved through an evolutionary algorithm and remeshing techniques.

4. Microfoams with 96% porosity reduce the net sputter yield by approximately 50% in W surfaces.

5. As time increases a redistribution of volume is found within the porous W foam.

REFERENCES

[1] Bruining, H. *Physics and Applications of Secondary Electron Emission: Pergamon Science Series: Electronics and Waves?a Series of Monographs* (Elsevier, 2016).

[2] Shih, A., Yater, J., Hor, C. & Abrams, R. Secondary electron emission studies. *Applied surface science* **111**, 251–258 (1997).

[3] Seiler, H. Secondary electron emission in the scanning electron microscope. *Journal of Applied Physics* **54**, R1–R18 (1983).

[4] Reimer, L. *Scanning electron microscopy: physics of image formation and microanalysis*, vol. 45 (Springer, 2013).

[5] Dunaevsky, A., Raitses, Y. & Fisch, N. Secondary electron emission from dielectric materials of a hall thruster with segmented electrodes. *Physics of Plasmas* **10**, 2574–2577 (2003).

[6] Raitses, Y., Smirnov, A., Staack, D. & Fisch, N. Measurements of secondary electron emission effects in the hall thruster discharge. *Physics of Plasmas* **13**, 014502 (2006).

[7] Phelps, A. & Petrovic, Z. L. Cold-cathode discharges and breakdown in argon: surface and gas phase production of secondary electrons. *Plasma Sources Science and Technology* **8**, R21 (1999).

[8] Zhurin, V., Kaufman, H. & Robinson, R. Plasma sources sci. technol. 0963-0252 https://doi. org/10.1088/0963-0252/8/1/021 8 (1999).

[9] Stangeby, P. C. *et al. The plasma boundary of magnetic fusion devices*, vol. 224 (Institute of Physics Publishing Bristol, 2000).

[10] Boyle, P., Ellingboe, A. & Turner, M. Electrostatic modelling of dual frequency rf plasma discharges. *Plasma Sources Science and Technology* **13**, 493 (2004).

[11] Kaganovich, I., Raitses, Y., Sydorenko, D. & Smolyakov, A. Kinetic effects in a hall thruster discharge. *Physics of Plasmas* **14**, 057104 (2007).

[12] Sydorenko, D., Smolyakov, A., Kaganovich, I. & Raitses, Y. Plasma-sheath instability in hall thrusters due to periodic modulation of the energy of secondary electrons in cyclotron motion. *Physics of Plasmas* **15**, 053506 (2008).

[13] Willis, R., Fitton, B. & Painter, G. Secondary-electron emission spectroscopy and the observation of high-energy excited states in graphite: Theory and experiment. *Physical Review B* **9**, 1926 (1974).

[14] Kishek, R. A., Lau, Y., Ang, L., Valfells, A. & Gilgenbach, R. Multipactor discharge on metals and dielectrics: Historical review and recent theories. *Physics of Plasmas* **5**, 2120–2126 (1998).

[15] Hobbs, G. & Wesson, J. Heat flow through a langmuir sheath in the presence of electron emission. *Plasma Physics* **9**, 85 (1967).

[16] Ahedo, E. & Escobar, D. Influence of design and operation parameters on hall thruster performances. *Journal of applied physics* **96**, 983–992 (2004).

[17] Curren, A. N. Carbon and carbon-coated electrodes for multistage depressed collectors for electron-beam devices?a technology review. *IEEE Transactions on Electron Devices* **33**, 1902–1914 (1986).

[18] Baglin, V. *et al.* The secondary electron yield of technical materials and its variation with surface treatments. Tech. Rep. (2000).

[19] Patino, M., Raitses, Y. & Wirz, R. Secondary electron emission from plasma-generated nanostructured tungsten fuzz. *Applied Physics Letters* **109**, 201602 (2016).

[20] Huerta, C., Patino, M. & Wirz, R. Secondary electron emission from textured surfaces. *Journal of Physics D: Applied Physics* **51**, 145202 (2018).

[21] Swanson, C. & Kaganovich, I. D. Modeling of reduced secondary electron emission yield from a foam or fuzz surface. *Journal of Applied Physics* **123**, 023302 (2018).

[22] Raitses, Y., Staack, D., Dunaevsky, A. & Fisch, N. Operation of a segmented hall thruster with low-sputtering carbon-velvet electrodes (2006).

[23] Ye, M. *et al.* Suppression of secondary electron yield by micro-porous array structure. *Journal of applied Physics* **113**, 074904 (2013).

[24] Yang, Q. *et al.* Nanostructured fuzz growth on tungsten under low-energy and high-flux he irradiation. *Scientific reports* **5**, 10959 (2015).

[25] Front matter. In BRUINING, D. H. (ed.) *Physics and Applications of Secondary Electron Emission*, Pergamon Science Series: Electronics and Waves–a Series of Monographs, iii – (Pergamon, 1962). URL `https://www.sciencedirect.com/science/article/pii/B9780080090146500016`.

[26] Dekker, A. & Van der Ziel, A. Theory of the production of secondary electrons in solids. *Physical Review* **86**, 755 (1952).

[27] Pivi, M. *et al.* Sharp reduction of the secondary electron emission yield from grooved surfaces. *Journal of Applied Physics* **104**, 104904 (2008).

[28] Möller, T. & Trumbore, B. Fast, minimum storage ray/triangle intersection. In *ACM SIGGRAPH 2005 Courses*, 7 (ACM, 2005).

[29] Chang, H.-Y., Alvarado, A. & Marian, J. Calculation of secondary electron emission yields from low-energy electron deposition in tungsten surfaces. *Applied Surface Science* **450**, 190 – 199 (2018). URL `http://www.sciencedirect.com/science/article/pii/S0169433218311176`.

[30] Streitwolf, H. Zur theorie der sekundärelektronenemission von metallen der anregungsprozess. *Annalen der Physik* **458**, 183–196 (1959).

[31] Kotera, M. A monte carlo simulation of primary and secondary electron trajectories in a specimen. *Journal of applied physics* **65**, 3991–3998 (1989).

[32] Gao, E., Nadvornick, W., Doerner, R. & Ghoniem, N. M. The influence of low-energy helium plasma on bubble formation in micro-engineered tungsten. *Journal of Nuclear Materials* **501**, 319 – 328 (2018). URL `http://www.sciencedirect.com/science/article/pii/S0022311517314769`.

[33] Gibson, L. J. & Ashby, M. F. *Cellular solids: structure and properties* (Cambridge university press, 1999).

[34] Baldwin, M., Doerner, R., Nishijima, D., Tokunaga, K. & Ueda, Y. The effects of high fluence mixed-species (deuterium, helium, beryllium) plasma interactions with tungsten. *Journal of Nuclear Materials* **390-391**, 886 – 890 (2009). URL `http://www.sciencedirect.com/science/article/pii/S0022311509002566`. Proceedings of the 18th International Conference on Plasma-Surface Interactions in Controlled Fusion Device.

[35] Lukkassen, D. & Meidell, A. Advanced materials and structures and their fabrication processes. *Narrik University College, Hin* (2003).

[36] García-Moreno, F. Commercial applications of metal foams: Their properties and production. *Materials* **9**, 85 (2016).

[37] Singh, S. & Bhatnagar, N. A survey of fabrication and application of metallic foams (1925–2017). *Journal of Porous Materials* **25**, 537–554 (2018).

[38] Appel, A. Some techniques for shading machine renderings of solids. In *Proceedings of the April 30–May 2, 1968, spring joint computer conference*, 37–45 (ACM, 1968).

[39] Whitted, T. An improved illumination model for shaded display. In *ACM SIGGRAPH Computer Graphics*, vol. 13, 14 (ACM, 1979).

[40] Chalmers, A., Reinhard, E. & Davis, T. *Practical parallel rendering* (CRC Press, 2002).

[41] Pelowitz, D. B. *et al.* Mcnpxtm user?s manual. *Los Alamos National Laboratory, Los Alamos* (2005).

[42] Wasastjerna, F. *et al. Using MCNP for fusion neutronics* (VTT, 2008).

[43] Meezan, N. B., Gascon, N. & Cappelli, M. A. Linear geometry hall thruster with boron nitride and diamond walls. In *Proc. 27th International Electric Propulsion Conference*, 01-039 (2001).

[44] Satonik, A. & Rovey, J. Modification of boron nitride ceramic to replicate hall effect thruster surface wear. In *50th AIAA Aerospace Sciences Meeting including the New Horizons Forum and Aerospace Exposition*, 198 (2012).

[45] Satonik, A. J., Rovey, J. L. & Hilmas, G. Effects of plasma exposure on boron nitride ceramic insulators for hall-effect thrusters. *Journal of Propulsion and Power* **30**, 656–663 (2014).

[46] Levchenko, I. *et al.* Recent progress and perspectives of space electric propulsion systems based on smart nanomaterials. *Nature communications* **9**, 879 (2018).

[47] Chang, H.-Y., Alvarado, A., Weber, T. & Marian, J. Monte carlo modeling of low-energy electron-induced secondary electron emission yields in micro-architected boron nitride surfaces. *Nuclear Instruments and Methods in Physics Research Section B: Beam Interactions with Materials and Atoms* **454**, 14 – 22 (2019).

[48] Agostinelli, S. *et al.* Geant4?a simulation toolkit. *Nuclear instruments and methods in physics research section A: Accelerators, Spectrometers, Detectors and Associated Equipment* **506**, 250–303 (2003).

[49] Allison, J. *et al.* Recent developments in geant4. *Nuclear Instruments and Methods in Physics Research Section A: Accelerators, Spectrometers, Detectors and Associated Equipment* **835**, 186–225 (2016).

[50] Jacobs, H., Freely, J. & Brand, F. A. The mechanism of field dependent secondary emission. *Physical Review* **88**, 492 (1952).

[51] Martinez-Sanchez, M. & Pollard, J. E. Spacecraft electric propulsion-an overview. *Journal of propulsion and power* **14**, 688–699 (1998).

[52] Goebel, D. M. & Katz, I. *Fundamentals of electric propulsion: ion and Hall thrusters*, vol. 1 (John Wiley & Sons, 2008).

[53] Huerta, C. E., Matlock, T. S. & Wirz, R. E. View factor modeling of sputter-deposition on micron-scale-architectured surfaces exposed to plasma. *Journal of Applied Physics* **119**, 113303 (2016).

[54] Ziegler, J. F., Ziegler, M. & Biersack, J. Srim the stopping and range of ions in matter (2010). *Nuclear Instruments and Methods in Physics Research Section B: Beam Interactions with Materials and Atoms* **268**, 1818 – 1823 (2010). URL `http://www.sciencedirect.com/science/article/pii/S0168583X10001862`. 19th International Conference on Ion Beam Analysis.

[55] Rosenberg, D. & Wehner, G. K. Sputtering yields for low energy he+, kr+, and xe+ion bombardment. *Journal of Applied Physics* **33**, 1842–1845 (1962).

[56] Stuart, R. V. & Wehner, G. K. Sputtering yields at very low bombarding ion energies. *Journal of Applied Physics* **33**, 2345–2352 (1962).

[57] Winters, H. F. & Sigmund, P. Sputtering of chemisorbed gas (nitrogen on tungsten) by lowenergy ions. *Journal of Applied Physics* **45**, 4760–4766 (1974).

[58] Doerner, R. P. Low-energy sputtering yields of tungsten and tantalum. *Journal of Vacuum Science & Technology A* **23**, 1545–1547 (2005).

[59] Tartz, M., Heyn, T., Bundesmann, C., Zimmermann, C. & Neumann, H. Sputter yields of mo, ti, w, al, ag under xenon ion incidence. *The European Physical Journal D* **61**, 587–592 (2011).

[60] Schmidt, M. & Lipson, H. Distilling free-form natural laws from experimental data. *science* **324**, 81–85 (2009).

[61] Devilliers, O. & Guigue, P. Faster triangle-triangle intersection tests (2002).

[62] Cignoni, P. *et al.* MeshLab: an Open-Source Mesh Processing Tool. In Scarano, V., Chiara, R. D. & Erra, U. (eds.) *Eurographics Italian Chapter Conference* (The Eurographics Association, 2008).

[63] Couëdel, L. *et al.* Formation, growth and behavior of dust particles in a sputtering discharge. In Šafránková, J. & Pavlů, J. (eds.) *15th Annual Student Conference, Week of Doctoral Students*, vol. Part II, 42 (MATFYZPRESS, Prague, Czech Republic, 2006). URL `https://hal.archives-ouvertes.fr/hal-00445233`.